The Planetary Science Journal, 7:156 (16pp), 2026 June https://doi.org/10.3847/PSJ/ae77fa

Triaxial Shapes and Densities of G!kún||'hòmdímà, Haumea, and Varda from Stellar Occultations

Benjamin Proudfoot[1], Will Grundy[2,3], Flavia Luane Rommel[1], Estela Fernández-Valenzuela[1], and Darin Ragozzine[4]
[1] Florida Space Institute, University of Central Florida, 12354, Research Parkway, Orlando, FL 32826, USA; benp175@gmail.com
[2] Lowell Observatory, 1400 W Mars Hill Road, Flagstaff, AZ 86001, USA
[3] Northern Arizona University, Department of Astronomy & Planetary Science, PO Box 6010, Flagstaff, AZ 86011, USA
[4] Brigham Young University Department of Physics & Astronomy, N283 ESC, Brigham Young University, Provo, UT 84602, USA
Received 2026 January 27; revised 2026 May 26; accepted 2026 May 26; published 2026 June 22

Abstract

The shapes and densities of midsized and large trans-Neptunian objects (TNOs) are pivotal for understanding a variety of important aspects of planet formation. In this work, we present a Bayesian shape modeling method that combines constraints from rotational light curves and satellite orbits to construct three-dimensional shape models of TNOs. We use it to reanalyze three stellar occultations of the TNOs (229762) G!kún||'hòmdímà (2007 UK_{126}), (136108) Haumea, and (174567) Varda. By assuming that their satellites (or rings) orbit in their respective equatorial planes, we are able to derive unique shape models for both G!kún||'hòmdímà and Haumea. Our derived shape for G!kún||'hòmdímà is spheroidal with $a = b = 329^{+4}_{-3}$ km and $c = 294^{+11}_{-10}$ km, with a system density $\rho = 1007^{+50}_{-49}$ kg m^{-3}. For Haumea, we find $a = 1061^{+87}_{-71}$ km, $b = 844^{+5}_{-7}$ km, and $c = 514^{+18}_{-19}$ km, providing $\rho = 2050^{+157}_{-152}$ kg m^{-3}. For Varda, after updating its mutual orbit with its satellite Ilmarë, we find that currently published data are unable to fully constrain its three-dimensional shape. Intriguingly, Varda's elongated limb appears to point toward its satellite at the time of the occultation. With a ∼2% chance of such an alignment happening randomly, this may be suggestive of a frozen-in tidal and/or rotational bulge. Our work emphasizes the importance of how external constraints can improve occultation analyses. With continued observations of rotational light curves, stellar occultations, and satellite orbits, these—and other—TNOs can have their shapes and densities further refined.

Unified Astronomy Thesaurus concepts: Trans-Neptunian objects (1705); Dwarf planets (419); Stellar occultation (2135); Asteroid occultation (71)

1. Introduction

Due to their large heliocentric distances, relatively little is known about the sizes, shapes, and densities of trans-Neptunian objects (TNOs). As the largest remnants of the process of planet formation—apart from the known planets—these bodies preserve clues to the conditions in the protoplanetary disk and the processes that governed planetary growth (A. Morbidelli & D. Nesvorný 2020). Understanding the shapes and densities of TNOs is key to understanding the formation and evolution of TNOs (W. B. McKinnon et al. 2008).

Shape provides interesting constraints on formation (Z. M. Leinhardt et al. 2010; M. A. Nelsen et al. 2025), collisional alteration (F. L. Rommel et al. 2023), and hydrostatic relaxation (J. L. Ortiz et al. 2017), while density can help to infer composition (W. M. Grundy et al. 2019), porosity (M. E. Brown 2013a), and thermal history (S. J. Desch et al. 2009). Measurements of bulk density also provide critical inputs into models of TNOs' internal structure (A. Guilbert-Lepoutre et al. 2020), which can inform the study of potential subsurface oceans (H. Hussmann et al. 2006) and the ability to generate/retain volatile species (E. L. Schaller & M. E. Brown 2007). The ensemble of shape and density measurements across the known TNOs also provides tight constraints on the timing and/or formation mechanisms of TNOs (C. J. Bierson & F. Nimmo 2019).

Despite their importance, high-precision size determinations remain available for only a small fraction of the known TNO population. With angular sizes of tens of mas (or less), TNO diameters are ∼unable to be directly measured from ground- or space-based telescopes, except in a few cases (e.g., S. A. Stern et al. 1997; M. W. Buie et al. 2010). Thermal radiometry with space-based observatories such as Spitzer and Herschel (E. Lellouch et al. 2013; T. Müller et al. 2020) has been successful in estimating effective diameters, but the resulting uncertainties can often be too imprecise to estimate densities (M. E. Brown & B. J. Butler 2017), while also requiring assumptions about the (often unknown) shape and spin-axis orientation (C. Kiss et al. 2019). On the other hand, mass measurements can be obtained fairly straightforwardly for any TNOs with a satellite/binary companion (e.g., W. M. Grundy et al. 2019). But for singleton objects, mass is currently impossible to measure (O. Fuentes-Muñoz et al. 2025).

The shapes of TNOs, which affect density measurements, are even more poorly constrained. Rotational light curves (RLCs) can constrain elongation and rotational properties (S. S. Sheppard et al. 2008; E. Fernández-Valenzuela 2022), but provide nonunique solutions, are affected by degeneracies between shape and albedo variegation, and require assumptions about surface scattering properties. Recently, work has been done to constrain the shapes of TNO binaries based on non-Keplerian orbital precession (B. C. N. Proudfoot et al. 2024b), but this is only

available for a few TNOs so far (B. C. N. Proudfoot et al. 2024a; M. A. Nelsen et al. 2025).

Shape is a critical input into understanding the role of hydrostatic equilibrium in TNOs (J. L. Ortiz et al. 2020). Generally, large TNOs have been assumed to be in (or at least near) hydrostatic equilibrium, which predict Maclaurin spheroid or Jacobi ellipsoid shapes if TNOs act like self-gravitating fluids (G. Tancredi & S. Favre 2008). Material strength and interparticle friction also play a role in the shapes of TNOs (K. A. Holsapple 2007). Similarly, the effects of nonhomogeneous density structures, which are expected in large differentiated TNOs, can also alter the shape of a TNO (N. Rambaux et al. 2017; E. T. Dunham et al. 2019). However, with such few measured three-dimensional shapes, little can be said about the relative roles of each of these effects. Thus, further determinations of TNO shapes are necessary to better understand the physical characteristics of these bodies.

One of the best techniques to understand both size and shape simultaneously is stellar occultations (J. L. Ortiz et al. 2020). Over the past few decades, with the Gaia stellar catalog (Gaia Collaboration et al. 2023) and TNO ephemerides (J. Desmars et al. 2015), occultations of many TNOs have now been observed. Unfortunately, occultations only provide an instantaneous view of the limb of a TNO, with further work required to derive a true three-dimensional shape and size. Multiple occultations, RLC constraints, and orientation constraints from rings and/or satellites can help to provide these more complex shape models.

In this work, we develop a new software tool to fit occultation chords to triaxial shape models constrained by satellite orbit poles and RLCs. We present our new software tool, named `occult3d`, in Section 2. Then, we apply it to G!kún||'hòmdímà, Haumea, and Varda in Sections 3, 4, and 5, where we derive triaxial shapes and densities. We then discuss population details and conclude in Section 6.

2. `occult3d`

Stellar occultations allow the measurement of the instantaneous elliptical limb of a TNO. While useful, one measurement of the limb alone cannot uniquely determine the three-dimensional shape of a TNO. With additional occultations, information derived from RLCs, or orientation constraints based on ring or satellite geometry, degeneracies can be broken providing a unique shape model. To allow for simultaneous use of all of these constraints, we have created `occult3d`, a publicly available Python-based software.

`occult3d` derives three-dimensional shape models of TNOs by casting the occultation fitting problem as a Bayesian parameter inference exercise. At its core, occultation chords (from an arbitrary number of events) are fit to three-dimensional shape models, while information about the target's orientation and RLC amplitude can be included as prior probabilities. Instead of χ^2 optimization or similar frequentist statistical methods, `occult3d` explores the model parameter space using a Markov Chain Monte Carlo (MCMC) approach. For simplicity, we choose the `emcee` sampler, an ensemble MCMC sampler that is widely used across a variety of fields (D. Foreman-Mackey et al. 2013). This allows `occult3d` to flexibly explore the entire parameter space and allows for easy identification of model degeneracies. With limited occultations, RLC knowledge, or other information, three-dimensional shape models can have significant degeneracies that provide nonunique shape models.

The forward model at the core of `occult3d` has eight free parameters (when analyzing a single occultation). Six of these parameters determine the three-dimensional shape (triaxial semiaxes a, b, c), orientation (pole direction α, δ), and rotational phase (ϕ) of the target. Two additional terms (f_c, g_c) provide the ephemeris offset of the limb's center on the plane of the sky. Based on the shape/orientation parameters, the elliptical limb profile of the target can be derived using the equations of P. Magnusson (1986). The χ^2 of the occultation chords (compared to the elliptical limb) can then be found by radial limb fitting (described in detail in, e.g., B. Sicardy et al. 2011; J. L. Ortiz et al. 2012).

Assuming independent, normally distributed errors, the Bayesian log-likelihood ($\mathcal{L}$) is proportional to $\frac{1}{2}\chi^2$. Priors can then be included to further refine shape models (e.g., M. E. Brown 2013b). In this version of `occult3d`, we focus on priors based on RLC knowledge and orientation constraints from rings and satellites.

First, we focus on RLC-derived constraints. Assuming that the RLC of a body is determined by the variation in projected limb area alone (i.e., neglecting albedo variegation and realistic scattering properties), the RLC amplitude of a triaxial TNO is given by the equation:

$$\Delta m = -\frac{5}{2}\log\left[\left(\frac{b}{a}\right)\left(\frac{(a/c)^2\cos^2\theta + \sin^2\theta}{(b/c)^2\cos^2\theta + \sin^2\theta}\right)^{1/2}\right], \quad (1)$$

where a, b, and c are the body's ellipsoidal semiaxes and θ is the polar aspect angle. A polar aspect angle of 0° (90°) corresponds to pole-on (equator-on) geometry. Therefore, with a known RLC amplitude, significant constraints on shape models can be found (e.g., J. L. Ortiz et al. 2017). When imposed in `occult3d`, RLC amplitude priors are normally distributed, taking an amplitude (Δm) as the mean and the (1σ) amplitude uncertainty ($\sigma_{\Delta m}$) as the scale. When light-curve measurements are taken at different times than occultations, some evolution of a body's aspect angle is expected, leading to slow changes in the RLC amplitude (e.g., E. Fernández-Valenzuela et al. 2019). To account for this, we apply the light-curve prior with the aspect angle of the body at the time of the light-curve observations, not the occultation. This allows our modeling to be as robust as possible to secular changes in the light curves of these bodies.

This formulation assumes that the entire RLC is caused by variations in the projected limb area, with no contributions from albedo variegation across a body's surface. Typically the surfaces of small bodies have uniform albedos, validating this assumption, though famous counterexamples do exist. Pluto notably has a high-amplitude RLC ($\Delta m \sim 0.3$; D. J. Tholen & E. F. Tedesco 1994) despite a spherical shape. Likewise, Haumea is known to have a dark red spot on its surface, though the extent of this feature is currently unconstrained (P. Lacerda et al. 2008).

Equation (1) also implicitly assumes the scattering behavior of the surfaces. Differences in scattering behavior and albedo variegation can radically change an RLC, biasing any inferred three-dimensional shape output. To account for these issues, judicious and parsimonious selection of priors is necessary. Although in this work we assume the formalism provided by Equation (1), where important, we revisit these assumptions and explore how altering them could lead to different shape

models. In particular, our discussion of Haumea in Section 4 provides a detailed examination of how scattering and albedo affect final shape models.

Although RLC amplitudes alone can narrow the range of allowable shape models, the constraints they place are limited without knowledge of the rotational phase at the time of occultation (ϕ). For some bodies with a high amplitude, well-measured RLC, it is possible to infer the rotational phase at the time of the occultation, but more often, the rotational phase is unknown. This is mostly because rotational periods are not known with the precision required to calculate the rotational phase at the moment of the occultation, unless an RLC has been taken relatively close in time to the occultation event. Thankfully, with the Bayesian approach used by `occult3d`, ϕ can be left as a free parameter, allowing the MCMC sampler to explore different values. In the future, with more numerous occultations, it will be possible to use a rotational period and single phase (for a given reference epoch) to eliminate these free parameters. This will be particularly important for cases like Quaoar, which has been observed during stellar occultations many times (e.g., G. Margoti et al. 2024).

Lastly, `occult3d` can include constraints on the orientation of the target. For some bodies, like Haumea, the presence of a ring naturally provides an independent measure of the body's pole orientation. Rings like those around Haumea and Quaoar, should lie very close to their parent's equatorial plane as any inclination will naturally be damped by differential precession caused by the TNO's nonspherical shape (M. S. Tiscareno 2013; F. Marzari 2020). Although less definitive, the presence of a satellite can also probe a body's orientation. For many large TNOs, satellites are expected to lie in (or near) their parent's equatorial plane (B. Sicardy et al. 2024). Confirmation of this alignment has yet to be made for most TNO-satellite systems, but where the alignment is independently measured, they tend to be well aligned (M. Brozović et al. 2015; B. C. N. Proudfoot et al. 2024a; F. Braga-Ribas et al. 2025). These constraints are further included as priors in `occult3d`, where the prior on the pole R.A./decl. (α, δ) is assumed to be normally distributed (see orbit fit in Section 5 and Appendix A).[5]

Although the dominant shape of large TNOs is expected to be overall triaxial, topography on the surface of TNOs (e.g., craters, mountains, etc.) can cause significant departures from an idealized triaxial shape (see, for example, F. L. Rommel et al. 2023). This can be especially important with chords with ultraprecise timing uncertainties. So as to not bias the triaxial shape model output by `occult3d`, an additional model uncertainty can be added to account for topography ($\sigma_{\rm topo}$). This uncertainty, which can be set arbitrarily based on physical expectations (e.g., T. V. Johnson & T. R. McGetchin 1973), is added in quadrature to the chord extremity uncertainties based on timing, similar to implementations in other works (B. E. Morgado et al. 2021; A. R. Gomes-Júnior et al. 2022; F. L. Rommel et al. 2023). We note that in this work, we use $\sigma_{\rm topo} = 0$ km, as our shape models generally provide good fit quality without it.

[5] α, δ are given by $\alpha = \Omega - 90°$ and $\delta = 90° - i$, where i, Ω are the inclination and longitude of the ascending node, in the equatorial frame.

To measure the goodness of fit for each of our `occult3d` fits, we use the mean normalized squared residuals, defined as

$$\mathrm{MNSR} = \frac{1}{N}\sum_i \left(\frac{y_{\rm obs} - y_{\rm model}}{\sigma_{\rm obs}}\right)^2, \quad (2)$$

where N is the number of chord extremities, $y_{\rm obs}$, $y_{\rm model}$ are the observed and modeled chord extremities, and $\sigma_{\rm total}$ is the total uncertainty in the chord extremity (i.e., including the user-specified topographic uncertainty). We use this in place of more traditional goodness-of-fit metrics (like reduced χ^2) as the number of effective degrees-of-freedom in our model is not well-defined given the presence of parameters that are strongly bounded by priors and/or strongly degenerate. The MNSR is equivalent to the average χ^2 of each chord extremity. For high-quality fits, we expect MNSR ~ 1, while poor-quality fits will have MNSR $\gg 1$. With MNSR $\ll 1$, uncertainties in the chord extremities are likely to be overestimated.

For simplicity, much of `occult3d` uses the functionality provided by the Stellar Occultation Reduction and Analysis (SORA) package (A. R. Gomes-Júnior et al. 2022). The tools provided by SORA are used for translating occultation chords to the sky plane, evaluating the χ^2 of trial limb profiles, and filtering solutions based on close negative chords. These tools are well-validated and used across a variety of stellar occultation work (e.g., F. L. Rommel et al. 2023; M. Kretlow et al. 2024; J. L. Rizos et al. 2025; F. L. Rommel et al. 2025). We point the reader to A. R. Gomes-Júnior et al. (2022) for a detailed explanation of occultation analysis with the SORA library.

`occult3d` has been made publicly available on GitHub,[6] alongside a citable Zenodo DOI: 10.5281/zenodo.20288143. There, full installation instructions and a quick start guide are provided. We also provide a full working example that reproduces the analysis we present in Section 3. We intend to add additional functionality to `occult3d` in the future, allowing for more complex photometric modeling, additional shape models, automated hydrostatic equilibrium analysis, fitting to multiple occultations, among others. We welcome contributions from the occultation community and hope that `occult3d` will enhance analysis of TNO occultations.

3. G!kún||'hòmdímà

G!kún||'hòmdímà (2007 UK_{126}) was observed during an occultation in 2014 November. A total of eight chords were obtained during the occultation campaigns, providing a well-constrained elliptical limb profile (G. Benedetti-Rossi et al. 2016; K. Schindler et al. 2017). Observations of G!kún||'hòmdímà's RLC found a low amplitude $\Delta m = 0.03 \pm 0.01$ (at average epoch 2011 October 30; A. Thirouin et al. 2014). In addition, G!kún||'hòmdímà has a satellite—G!ò'é !hú—which can place a strong constraint on the orientation of G!kún||'hòmdímà if we assume it is on an equatorial orbit (W. M. Grundy et al. 2019).

Using `occult3d`, we fit a three-dimensional shape model to G!kún||'hòmdímà's occultation chords. These chords are compiled in Table B1, along with all chords for subsequent analyses. The results of our shape fitting are displayed in Table 1, along with the MNSR measuring the goodness of fit.

[6] https://github.com/benp175/occult3d

Table 1
Triaxial Shape Fitting Results

	G!kún‖'hòmdímà Triaxial	G!kún‖'hòmdímà Maclaurin	Haumea	Varda (best fit)
Best-fit MNSR	1.31	1.36	1.41	0.86
		Priors		
a (km)	$0 < a < 5000$	$0 < a < 5000$	$0 < a < 5000$	$0 < a < 5000$
b (km)	$0 < b < a$	$0 < b < a$	$0 < b < a$	$0 < b < a$
c (km)	$0 < c < b$	$0 < c < b$	$0 < c < b$	$0 < c < b$
α (deg)	20.6 ± 1.5	20.6 ± 1.5	285.1 ± 0.5	272.6 ± 1.5
δ (deg)	46.25 ± 0.32	46.25 ± 0.32	−10.6 ± 1.2	−10.8 ± 2.0
ϕ (deg)	⋯	⋯	75.6 ± 3.6	⋯
f_c (km)	⋯	⋯	⋯	⋯
g_c (km)	⋯	⋯	⋯	⋯
Δm (mag)	0.03 ± 0.01	⋯	0.32 ± 0.10	⋯
		Fitted Parameters		
a (km)	336^{+8}_{-6}	329^{+4}_{-3}	1061^{+87}_{-71}	389
b (km)	325^{+5}_{-7}	⋯	844^{+5}_{-7}	353
c (km)	295^{+11}_{-11}	294^{+11}_{-10}	514^{+18}_{-19}	248
f_c (km)	11^{+4}_{-4}	11^{+4}_{+4}	-130^{+14}_{-13}	−20
g_c (km)	23^{+7}_{-7}	-21^{+6}_{-7}	-174^{+9}_{-10}	−128
		Derived Parameters		
r_{vol} (km)	318^{+5}_{-5}	317^{+5}_{-4}	772^{+20}_{-19}	324
ρ (kg m^{-3})	997^{+58}_{-54}	1007^{+50}_{-49}	2050^{+157}_{-152}	1726
c / a	$0.88^{+0.04}_{-0.04}$	$0.89^{+0.04}_{-0.03}$	$0.49^{+0.04}_{-0.04}$	0.64
b / a	$0.96^{+0.01}_{-0.01}$	⋯	$0.79^{+0.06}_{-0.06}$	0.91

Note. Fitting for Varda does not return a unique shape model, so we show the best-fit model found, though we point out that the c-axis is ∼uncorrelated with goodness of fit. Both pole orientation angles are referenced to the J2000 equatorial coordinate system and are defined as the direction of the spin angular momentum in a right-handed coordinate system. Ephemeris centers are referenced to the NIMAv11, JPL#125, and NIMAv14 ephemerides for G!kún‖'hòmdímà, Haumea, and Varda, respectively (for more information on NIMA, see J. Desmars et al. 2015). Priors are implemented as Gaussian distributions with mean and standard deviation as given. Where no data is given for priors, priors are not implemented. For fitted parameters, no data are given for quantities that are not applicable (e.g., b-axis in the Maclaurin model since $b = a$, by definition). Light-curve priors take into account any change in aspect angle between the light-curve measurements and the occultation. Density (ρ) is the system density for G!kún‖'hòmdímà and Varda, but for Haumea, it is solely Haumea's density (i.e., no satellite contribution).

We also show the posterior for our analysis as a corner plot in Figure 1. With such a low-amplitude RLC, the resulting shape model is nearly azimuthally symmetric ($a \approx b$) with $a = 336^{+8}_{-6}$ km, $b = 325^{+5}_{-7}$ km, and $c = 295^{+11}_{-11}$ km. This yields a volumetric radius (the radius of a sphere with identical volume) of $r_{vol} = 318^{+5}_{-5}$ km. We compare the three-dimensional shape model and occultation chords in Figure 2.

Using the system mass of (136.1 ± 3.3) × 10^{18} kg (W. M. Grundy et al. 2019), we can also derive the system density. Based on a size ratio of 4.45 ± 0.08 between G!kún‖'hòmdímà and G!ò'é !hú (W. M. Grundy et al. 2019), our triaxial shape yields a density of $\rho = 997^{+58}_{-54}$ kg m^{-3} for the system, when assuming that G!ò'é !hú has an equivalent albedo, shape, and density.

Our derived shape model is very close to a spheroidal ($a/b = 1$) due to the low RLC amplitude and low subobserver geometry. Therefore, we should also consider that, with such a small RLC amplitude, the photometric variations may be due to albedo variegations on the surface of G!kún‖'hòmdímà, rather than a triaxial shape. In this case, `occult3d` gives $a = b = 329^{+4}_{-3}$ km and $c = 294^{+11}_{-10}$ km ($c/a = 0.89^{+0.04}_{-0.03}$) and a density of $\rho = 1007^{+50}_{-49}$ kg m^{-3}. This model provides a similar likelihood as the triaxial model.

Although using equilibrium figures is an imperfect way to understand the shapes of TNOs (see K. A. Holsapple 2007), their use provides a physically motivated model that can provide some guidance in data-limited regimes. To understand whether the spheroidal shape of G!kún‖'hòmdímà is consistent with being a Maclaurin spheroid in hydrostatic equilibrium, we can compare our shape model to that expected of a fluid at a given rotation and density. Using the Chandrasekhar formalism (S. Chandrasekhar 1987), a Maclaurin spheroid will satisfy the following equation:

$$\frac{\Omega^2}{\pi G\rho} = \frac{2\sqrt{1-e^2}}{e^3}(3-2e^2)\arcsin e - \frac{6}{e^2}(1-e^2), \quad (3)$$

where Ω is the angular velocity, G is the gravitational constant, ρ is the density, and $e^2 = 1 - c^2/a^2$. Numerically solving this equation for Ω, given our measured shape and density, we find G!kún‖'hòmdímà is in/near hydrostatic equilibrium when/if its rotational period is between 9.8 and 14.5 hr. This is very close to the 11.05 h period reported in the literature, though other possible period aliases exist (A. Thirouin et al. 2014). This provides compelling evidence—though not conclusive given the uncertainty in rotation period—that if G!ò'é !hú orbits in G!kún‖'hòmdímà's equatorial plane, G!kún‖'hòmdímà is likely in (or nearly in) hydrostatic equilibrium. Alternatively, it could retain a hydrostatic equilibrium shape that was frozen-in at an earlier epoch (potentially even at formation). Further confirmation of the shape model and better RLC periods can provide more insight into this possibility.

The success of our modeling approach shows that even a single occultation can help to refine the triaxial shape of

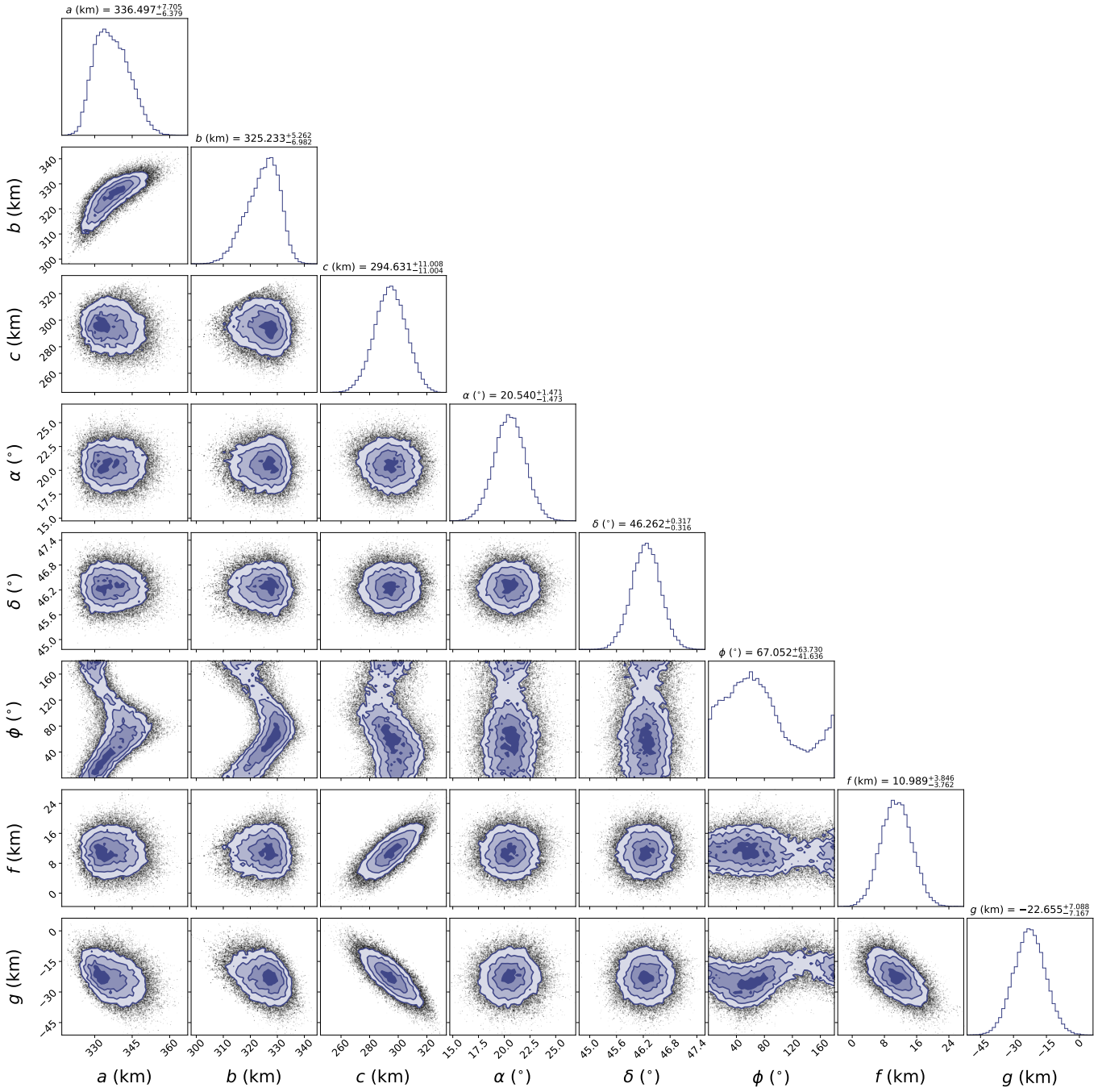

Figure 1. A corner plot showing the triaxial shape model derived for G!kún||'hòmdímà. Marginal (one-dimensional) parameter posterior distributions are shown along the tops of each column, while joint (two-dimensional) parameter distributions for each pair of parameters are shown as contour plots. Contours show the 0.5σ, 1σ, 1.5σ, and 2σ confidence intervals. Black points show individual samples from the MCMC chain.

midsized TNOs when combined with RLCs and reasonable assumptions about the orientation of satellite orbits.

Confirming our assumptions about G!kún||'hòmdímà's orientation will require substantial dedication of observation resources. Although RLCs can help to distinguish orientation solutions (e.g., S. C. Tegler et al. 2005; E. Fernández-Valenzuela et al. 2017, 2019), the low-amplitude RLC of G!kún||'hòmdímà and slow sky movement make this process nearly impossible. In addition, if the light curve is due to albedo variegation, the RLC amplitude changes due to changing aspect angle can be complex, especially if albedo features are localized.

In future occultations, our spheroidal shape model predicts that the limb shape will be similar to that previously observed, with only small changes due to G!kún||'hòmdímà's heliocentric motion. Another observation of a similar limb shape can help to confirm our shape model, but cannot independently measure the pole orientation.

One route forward is to observe the precession of G!ò'é !hú's orbit. Nodal precession can reveal the obliquity of the primary (with respect to the satellite orbit), but cannot provide a unique pole orientation (B. C. N. Proudfoot et al. 2024b). Given the shape we derive, we expect that the nodal

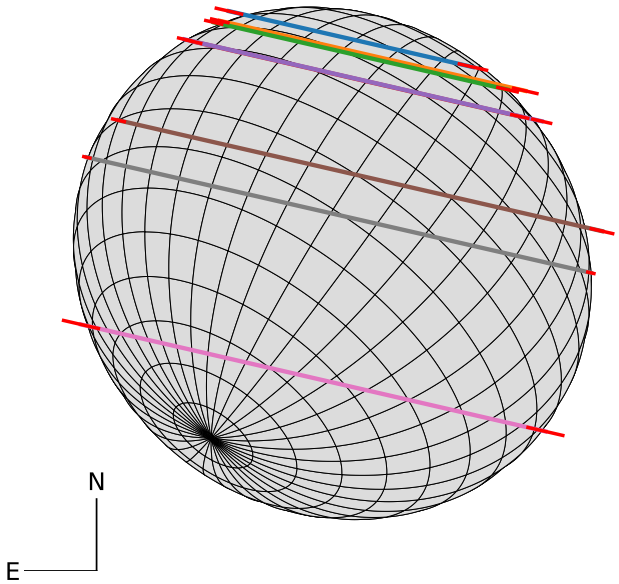

Figure 2. Our best-fit triaxial shape model for G!kún||'hòmdímà. Colored lines show the various occultation chords detected during the 2014 stellar occultation (G. Benedetti-Rossi et al. 2016; K. Schindler et al. 2017), while the red line tips show the uncertainty in the start and end of the occultation chords. This best-fit model corresponds to a shape of $a = 339$ km, $b = 326$ km, and $c = 298$ km.

precession rate is $\sim$1°–3° yr^{-1}, with a total precession period of $\sim$100–300 yr. This may be detectable with new astrometric measurements of the system as the earliest observations of the system date to 2008. With a known shape, even a nondetection of nodal precession can provide strong constraints on the pole orientation of G!kún||'hòmdímà.

We encourage continued observations of G!kún||'hòmdímà–G!ò'é !hú, which will further refine the system's density, shapes, mutual orbits, and orientations.

The inferred bulk density for G!kún||'hòmdímà–G!ò'é !hú —$\rho = 1007^{+50}_{-49}$ kg m^{-3}—is quite low for its size. Assuming it has a similar composition to other large TNOs (typically with densities $\sim$1800 kg m^{-3}), such a low density requires a porosity of $\sim$45% (for further discussion, see W. M. Grundy et al. 2019). This seems to stand in contrast to its fairly regular (near) hydrostatic equilibrium shape, as the same physics that produces such equilibrium shapes, gravity overcoming viscosity/strength, will tend to compress pores. The presence of a small presumably collisionally formed moon, like those around other large TNOs (A. C. Barr & M. E. Schwamb 2016), also would suggest an extensive collisional history, which should provide some compaction of the upper 10 s of km of the surface (C. Milbury et al. 2015; C. J. Bierson & F. Nimmo 2019).

The case of G!kún||'hòmdímà is similar to that of Uni (provisionally designated 2002 UX$_{25}$), which has a small satellite, similar size, and low bulk density—though its density is only inferred from thermal measurements (M. E. Brown 2013a; M. E. Brown & B. J. Butler 2017). Just larger than this size range, densities appear to rapidly increase (see Section 6), a transition that has proved difficult to explain (C. J. Bierson & F. Nimmo 2019; S. Loveless et al. 2022; M. H. Cañas et al. 2024). Perhaps more complex models, which may simultaneously account for pore space collapse, collisions, internal melting, possible compositional differences (like those proposed by M. H. Cañas et al. 2024), and/or other complex geophysical mechanisms, will provide more insight into the formation of these fascinating transitional bodies.

4. Haumea

In 2017, a multichord occultation of Haumea was captured by almost a dozen telescopes over Europe (J. L. Ortiz et al. 2017). From this event, a three-dimensional shape of Haumea was successfully derived based on the orientation of Haumea's rings and its light curve, assuming that Haumea was at its light-curve minimum. However, as pointed out by E. T. Dunham et al. (2019), the assumption of minimum rotational phase can significantly change the implied shape of Haumea and may not have been fully justified. Although Haumea was certainly near its minimum, photometry from around the time of the occultation shows that occultation occurred briefly before rotational minimum (see Extended Data Figure 6 in J. L. Ortiz et al. 2017). Here, we conduct a full reanalysis of the occultation data using `occult3d`.

To constrain shape models of Haumea, we perform a very similar analysis as J. L. Ortiz et al. (2017), but instead allow the rotational phase to vary around its expected value. Based on Extended Data Figure 6 from J. L. Ortiz et al. (2017), which shows the RLC of Haumea phased to the time of occultation, the occultation occurred at a phase of 0.04 $\pm$ 0.01 (or $14\overset{\circ}{.}4 \pm 3\overset{\circ}{.}6$) before minimum. Hence, in our `occult3d` fits, we place a prior of $\phi = 90° - (14.4 \pm 3.6)°$, where 90° corresponds to the minimum.

As previously done, we leverage the orientation of Haumea's ring to constrain Haumea's pole orientation. Rings around oblate bodies like Haumea quickly have any inclination damped, which minimizes differential precession that can increase collisional activity (M. S. Tiscareno 2013; F. Marzari 2020). Haumea's satellites are too far away to significantly perturb ring particles and play practically no role in the orientation of the rings, making this a very safe assumption (e.g., F. Marzari 2020). Hence, we place priors of $\alpha = 285\overset{\circ}{.}1 \pm 0\overset{\circ}{.}5$ and $\delta = -10\overset{\circ}{.}6 \pm 1\overset{\circ}{.}2$ to match the ring orientation found in J. L. Ortiz et al. (2017).

Haumea's RLC amplitude has been well-studied over the decades since its discovery (e.g., P. Lacerda et al. 2008; A. C. Lockwood et al. 2014). Importantly, A. C. Lockwood et al. (2014) studied Haumea's RLC with the Hubble Space Telescope (HST), which provided resolved photometry of the Haumea system and was able to resolve Haumea's RLC without dilution from its satellites. This RLC has an amplitude of $\Delta m = 0.32$ (on 2009 February 4); however, it is unclear how much of the amplitude is from shape and/or albedo. Indeed, the two RLC minima have a difference of $\sim$0.05 mag.

In addition to this, Equation (1) cannot account for more realistic surface properties; A. C. Lockwood et al. (2014) point out that when using a more realistic surface, the required axis ratios are less extreme than would be expected from Equation (1) alone. For example, they suggest a $b/a = 0.80 \pm 0.01$ using a photometric model based on Uranus' moon Ariel to match $\Delta m = 0.32 \pm 0.006$ mag. In comparison, Equation (1) gives $\Delta m = 0.24 \pm 0.01$ mag for those axis ratios (when using the same aspect angle). This suggests that uncertainties of $\sim$0.1 mag on the RLC amplitude could be present. Ideally, we could instead use a realistic photometric model to more accurately model the photometric behavior, but we defer this to future work.

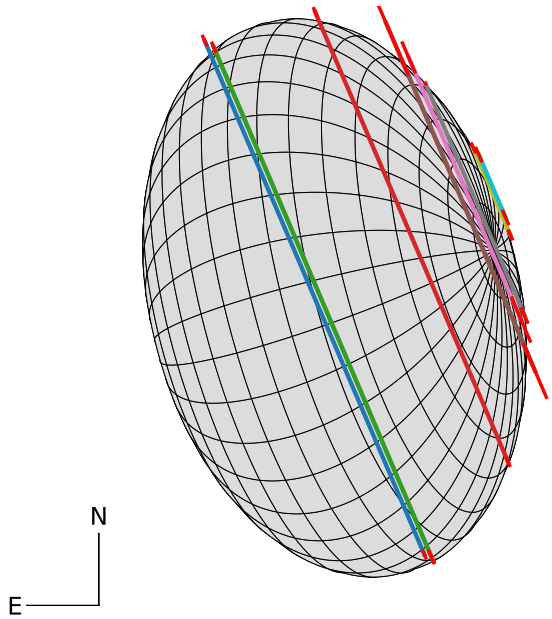

Figure 3. Best-fit shape model of Haumea, in the style of Figure 2. The shape model shown here corresponds to a triaxial shape with $a = 1072$ km, $b = 842$ km, and $c = 515$ km. Occultation chords are those given in J. L. Ortiz et al. (2017).

Alternatively, RLC constraints could be eliminated altogether by fitting multiple occultations simultaneously, but no such data are publicly available. To remain as conservative as possible in our shape modeling and account for both the uncertainties in the shape/albedo degeneracy and the lack of a realistic photometric model, we place a prior of $\Delta m = 0.32 \pm 0.10$ mag. This may be overly pessimistic, but it more precisely accounts for our lack of knowledge about Haumea and its RLC. When using this prior, we find that the occultation chords provide a slightly better fit when assuming a lower RLC amplitude around ∼0.24 mag, suggesting that $\Delta m = 0.32$ mag may indeed be too large (when assuming Equation (1)).

Using all these constraints, we fit a triaxial model to Haumea based on the 2017 occultation chords (all chords are presented in Table B1). Our results are shown in detail in Table 1. We found a triaxial shape with $a = 1061^{+87}_{-71}$ km, $b = 844^{+5}_{-7}$ km, and $c = 514^{+18}_{-19}$ km. We plot our best-fit model in Figure 3. This yields a volume-equivalent radius of $r_{vol} = 772^{+20}_{-19}$ km. Combined with the most recent measurement of Haumea's mass, $(3952 \pm 11) \times 10^{18}$ kg (B. C. N. Proudfoot et al. 2024a), this yields a total bulk density of Haumea of 2050^{+157}_{-152} kg m^{-3}.

Compared to J. L. Ortiz et al. (2017; $a = 1161 \pm 30$ km, $b = 852 \pm 4$ km, $c = 513 \pm 16$ km, $r_{\rm vol} = 798 \pm 6$ km, and $\rho = 1857 \pm 42$ kg m^{-3} when using the updated mass), our solution is broadly similar in overall triaxial geometry but does show systematic differences in the inferred axis lengths. These differences are primarily driven by two methodological choices: our treatment of rotational phase as a free parameter and differences in the adopted photometric constraints and uncertainty estimates. One of `occult3d`'s strengths is its ability to fully propagate uncertainties associated with model assumptions (e.g., rotational phase or spin-axis geometry), resulting in more realistic parameter uncertainties in the present analysis.

The triaxial shape we derive roughly matches the model suggested by hydrostatic equilibrium of a two-layer differentiated model of Haumea (E. T. Dunham et al. 2019), albeit with a slightly smaller c-axis. If borne out by future occultations, this smaller c-axis could indicate that Haumea is slightly out of hydrostatic equilibrium. Alternatively, a more complicated internal model with additional layers—possibly a subsurface ocean—could provide a better match to Haumea's shape.

Unfortunately, Haumea is in a sparse star field, making occultations relatively rare occurrences. However, even just a few positive occultation chords will enable far better constraints on Haumea's triaxial shape and may enable analyses without assumptions about Haumea's RLC, sidestepping any issues stemming from inaccurate photometric models. Future occultations will also provide an opportunity to further refine the ring orientation, further improving shape modeling efforts.

5. Varda

5.1. Updating the Mutual Orbit

Here, we provide an updated orbit fit for the Varda-Ilmarë binary system. Although an orbit solution was derived in W. M. Grundy et al. (2015), that work provided two mirror-ambiguous orbit solutions with different orbit pole directions. With enough time since the last set of observations, the breaking of this mirror ambiguity is now possible.

To do this, we acquired three Keck observations of Varda and Ilmarë from 2021 to 2024 using the laser guide star adaptive optics system (P. L. Wizinowich et al. 2006) with the NIRC2 camera.[7] Observations were taken in the infrared H filter, with wavelengths between ∼1.48 and 1.77 μm, and were dithered to allow for sky subtraction. Astrometry was extracted using well-validated methods described in the literature (e.g., W. M. Grundy et al. 2015). In addition to these new observations, we use the available relative astrometry in the literature (W. M. Grundy et al. 2015); our entire dataset is shown in Table 2.

Using these new observations, orbit fitting was able to rule out the retrograde orbit at 6σ confidence. With a single orbit solution, we performed a more detailed orbit fit using `MultiMoon`, a Bayesian orbit fitter designed for fitting TNO binary orbits (D. Ragozzine et al. 2024). We used the Keplerian orbit fitting module, see D. Ragozzine et al. (2024) and B. C. N. Proudfoot et al. (2024b) for further description of how `MultiMoon` functions. Our fits were run with 960 walkers for 45,000 total steps (20,000 burn-in, 5000 postpruning burn-in, and 20,000 sampling). Convergence of the fits was assessed based on posterior smoothness, best-fit sample quality, and inspection of walker trace plots. The orbit residuals and posterior distribution are shown in Appendix A.

Our final orbit solution is shown in Table 3. Although slightly different from the past orbit solution, this is not unexpected given the new data. Interestingly, our best-fit orbit solution has a χ^2_ν (χ^2 per degree of freedom) of ∼1.8. This confirms previous findings that Varda-Ilmarë's mutual orbit appears to have a significant non-Keplerian component, possibly due to the nonspherical shape of Varda (or Ilmarë; B. C. N. Proudfoot et al. 2024b). We leave further analysis of the non-Keplerian component of the orbit to future work.

[7] https://www2.keck.hawaii.edu/inst/nirc2

Table 2
Observed Astrometric Positions of Ilmarë

Julian Date	Date	Telescope/Instrument	$\Delta\alpha \cos\delta$ (arcsec)	$\sigma_{\Delta\alpha\cos\delta}$ (arcsec)	$\Delta\delta$ (arcsec)	$\sigma_{\Delta\delta}$ (arcsec)
2454947.91380	2009-04-26	HST/WFPC2	+0.12311	0.00334	−0.01033	0.00201
2455411.77394	2010-08-03	Keck/NIRC2	−0.09206	0.00200	−0.10862	0.00200
2455411.84777	2010-08-03	Keck/NIRC2	−0.08012	0.00200	−0.11149	0.00200
2455439.72274	2010-08-31	HST/WFC3	−0.13093	0.00097	−0.00172	0.00246
2455441.04295	2010-09-01	HST/WFC3	−0.02228	0.00131	−0.13318	0.00137
2455467.09059	2010-09-27	HST/WFC3	−0.00562	0.00467	+0.13799	0.00172
2455752.29017	2011-07-09	HST/WFC3	+0.08235	0.00858	−0.11167	0.00413
2456020.03911	2012-04-02	Gemini/NIRI	−0.11187	0.00300	+0.07594	0.00300
2456053.96807	2012-05-06	Gemini/NIRI	−0.05069	0.00300	+0.12971	0.00300
2456141.85712	2012-08-02	Gemini/NIRI	−0.10084	0.01354	−0.07780	0.00618
2456404.98806	2013-04-22	Gemini/NIRI	−0.08404	0.00300	+0.09796	0.01080
2456486.75571	2013-07-13	Gemini/NIRI	−0.12196	0.00332	−0.08097	0.00786
2459453.80128	2021-08-27	Keck/NIRC2	−0.14815	0.00300	−0.00494	0.00300
2460537.83575	2024-08-15	Keck/NIRC2	+0.15285	0.00300	+0.01362	0.00300
2460575.74686	2024-09-22	Keck/NIRC2	−0.12305	0.00391	−0.07866	0.00300

Note. Observations from 2013 and before are taken verbatim from W. M. Grundy et al. (2015).

Table 3
Keplerian Orbit Solution for Varda-Ilmarë

Parameter		Posterior
Fitted parameters		
System mass (10^{18} kg)	$M_{\rm sys}$	$267.5^{+4.9}_{-4.8}$
Semimajor axis (km)	a	4815^{+29}_{-29}
Eccentricity	e	$0.016^{+0.004}_{-0.004}$
Inclination (deg)	i	$77.4^{+1.9}_{-1.9}$
Argument of periapsis (deg)	ω	307^{+15}_{-19}
Longitude of the ascending node (deg)	Ω	$2.6^{+1.5}_{-1.5}$
Mean anomaly at epoch (deg)	$\mathcal{M}$	145^{+19}_{-15}
Derived parameters		
Orbit period (day)	$P_{\rm orb}$	$5.750824^{+0.000016}_{-0.000016}$
Orbit pole R.A. (deg)	$\alpha_{\rm orb}$	$272.6^{+1.4}_{-1.5}$
Orbit pole decl. (deg)	$\delta_{\rm orb}$	$-10.8^{+2.0}_{-1.9}$

Note. Reported values represent the median value, and uncertainties are based on 16th and 84th percentiles. All fitted angles are relative to the J2000 ecliptic plane on Varda-centric JD 2455300 (2010 April 14 12:00 UT), except for R.A. and decl. values, which are referenced to the J2000 equatorial coordinate system.

5.2. Occultation Fitting

In 2018, Varda was observed during a stellar occultation over the USA. Five chords from this event have been published (D. Souami et al. 2020), with an additional 15 positive chords reported in a conference abstract, but have not yet been published (K. Schindler et al. 2019). Even with the five publicly available chords, valuable constraints can be placed on Varda's size and shape. Combining these occultation chords with constraints from Ilmarë's orbit pole and Varda's RLC, a possible triaxial shape model can be derived.

First looking to priors from Varda's RLC, A. Thirouin et al. (2014) used 4 yr worth of photometric data in an attempt to recover Varda's RLC period. The best fit provided a single-peaked rotation period of 5.91 hr and amplitude of 0.02 ± 0.01 mag (at average epoch 2011 July 15), but with many similar peaks in the periodogram, confidence of that period is relatively low. Other analyses showed similar periods (and aliases) but with higher RLC amplitudes of 0.06 ± 0.02 mag (A. Thirouin et al. 2010). Given the relatively large size ratio (comparable to Pluto–Charon), tidal synchronization should happen relatively quickly, especially at the small semimajor axis of the binary (A. Thirouin et al. 2014). Salacia-Actaea, another similarly sized TNO binary, was recently discovered to be tidally synchronized despite early indications that showed a rapid ∼6.5 hr RLC period (C. Collyer et al. 2025). With no definitive rotation solution and a pole-on orbit of Ilmarë, we do not place any constraints on either the RLC amplitude or the rotational phase.

We place a prior on Varda's pole orientation to match the orientation of Ilmarë's orbit (see Table 3). In the case of a tidally evolved Varda and Ilmarë, this assumption is well-justified as it is the tidal end state of any binary system (P. Hut 1980). Even if not fully tidally evolved, alignment of the orbit and rotational axes is likely (B. Sicardy et al. 2024).

Using `occult3d`, we fit a triaxial shape model to Varda. Although our best-fit solution (shown in Table 1) provides a reasonable shape model with $a = 389$ km, $b = 353$ km, and $c = 248$ km (Figure 4), a wide range of shape models are allowable (hence why we only provide the best-fit values). Good-fit shape models typically have $b/a \sim 0.9$, although a nonunity value is favored only at $\sim 1.5\sigma$. Our models, however, have unconstrained values for c / a. This is due to Varda's nearly pole-on orientation (i.e., we view Varda along the c-axis) making it difficult to infer any information along the line of sight. A pole-on geometry is indeed consistent with the low apparent photometric variability (A. Thirouin et al. 2014).

Based on the reported occultation chords, D. Souami et al. (2020) provided a detailed analysis of Varda's shape under the assumption of a Maclaurin spheroidal shape. They found that a Maclaurin shape seemed to be consistent with the occultation limb if one of the mirror orbit solutions was chosen. Unfortunately, this orbit solution has now been conclusively ruled out. If Varda is indeed aligned with Ilmarë's orbit, Varda's apparent elongation ($a > b$) suggests a triaxial, rather

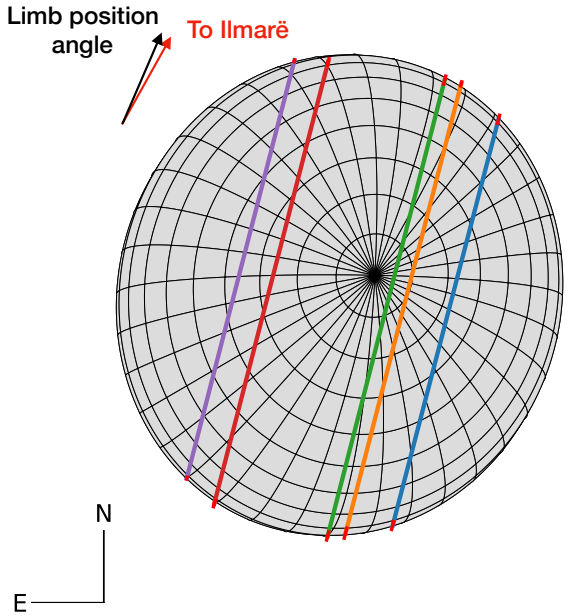

Figure 4. Best-fit shape model for Varda, in the style of Figure 2. The shape model shown here corresponds to a triaxial shape with $a = 389$ km, $b = 353$ km, and $c = 248$ km. We point out that a wide range of shape models—especially those with a wide range of c / a ratios—are allowable given the current constraints. The red arrow points toward the direction of Ilmarë during the occultation, while the black arrow points to the best-fit position angle (though with an uncertainty of 8°). Occultation chords are those given in D. Souami et al. (2020).

than spheroidal, shape. If rotating rapidly, Varda's triaxial shape could be due to rotational deformation.

A rotating Jacobi ellipsoid in hydrostatic equilibrium will satisfy the following relationship:

$$\frac{a^2b^2}{b^2 - a^2}[f(a^2, b^2, c^2, a^2) - f(a^2, b^2, c^2, b^2)] = c^2 f(a^2, b^2, c^2, c^2), \quad (4)$$

where a, b, and c are the semiaxes of the ellipsoid and f is the elliptic integral:

$$f(x, y, z, p) = \frac{3}{2}\int_0^\infty \frac{dt}{(t + p)\sqrt{(t + x)(t + y)(t + z)}} \quad (5)$$

(G. H. Darwin 1886; I. Thompson 2011), where t is the quantity being integrated over and p is an arbitrary input. Numerically solving this equation using our best fit $a = 389$ km and $b = 353$ km, we find $c = 216$ km. This yields a system density of 1900 kg m^{-3}, when using a diameter ratio between Varda and Ilmarë of 1.95 (W. M. Grundy et al. 2015) and the system mass from Table 3. A Jacobi ellipsoid satisfies:

$$\frac{\omega^2}{\pi G\rho} = \frac{4abc}{3(a^2 - b^2)}[a^2 f(a^2, b^2, c^2, a^2) - b^2 f(a^2, b^2, c^2, b^2)], \quad (6)$$

which allows calculation of the rotation period required for such a Jacobi ellipsoid. We find our best fit would need to rotate with a period of ∼4.5 hr to be explained by rotational deformation. With such an extreme shape, the light curve would likely be dominated by the triaxial shape, as such the single-peaked light-curve period would be half this value. This period is much shorter than that derived by A. Thirouin et al. (2014), and the density implied appears somewhat too high for an object the size of Varda (see Figure 5). We note that our shape models provide a range of allowable a and b values (and therefore hydrostatic c values), so solutions with reasonable density and rotation period may exist.

Tidal deformation due to Ilmarë can also alter Varda's shape. The equilibrium figure of a binary (assuming fluid bodies) in synchronous rotation has its surface defined by a Roche ellipsoid (É. Roche 1850; S. Chandrasekhar 1963). Based on the sequences of Roche ellipsoids tabulated by G. Leone et al. (1984), with a mass ratio $M_2/M_1 \approx 0.08$, rotation/orbital period of 5.75 days and density of ∼1500 kg m^{-3}, we estimate Varda's current tidal deformation at $b/a > 0.99$—a trivial amount. As such, we can confidently rule out tidal forces at their present strength as the source of Varda's possible triaxial shape.

Alternatively, Varda could have a nonhydrostatic equilibrium shape. We note that, at the time of the 2018 occultation, Varda's long (a) axis appears to point toward Ilmarë (see Figure 4). The projected two-dimensional elliptical limb of Varda has a position angle of 67° ± 8° (D. Souami et al. 2020), while Ilmarë is at a position angle of 60.°8 ± 0.°7. The probability of such a close alignment (or better) happening at random—if Varda is nonsynchronously rotating—is ∼2%. Such an alignment is the minimum energy state expected of a fully tidally evolved system. If Varda is rotating synchronously, as we suggest, the ellipticity of Varda's limb could represent a frozen-in shape (i.e., a fossil bulge) from a time when it had a much more rapid rotation (allowing it to take on a triaxial shape) and/or a more pronounced tidal bulge. We do note that nonfluid shapes are also possible when granular physics, internal friction, nonhomogeneous density distributions, and other factors are taken into account (K. A. Holsapple 2007; N. Rambaux et al. 2017). A full accounting of these effects requires a better shape model for Varda.

Additional RLC monitoring and observations of occultations will provide further clarification on Varda's possible triaxial shape and fossil bulge. Just a single multichord occultation with another apparent alignment would provide strong evidence for (or against) a fossil bulge. Similarly, additional occultation chords from the 2018 event may show Varda's elliptical limb in more detail and could probe the edges of the limb where more information about the c-axis is available (see Figure 4).

Given the lack of a unique shape model, a precise measure of Varda's volumetric radius or density cannot be derived. With a pole-on geometry—if Varda is indeed aligned with Ilmarë's orbital plane—it will be difficult to probe Varda's c-axis. Although idealized models—like Jacobi ellipsoids—can provide theoretical constraints, they rely on well-measured RLCs and assume hydrostatic equilibrium. Thus, it seems unlikely that *empirical* shape models for Varda will improve considerably without either remote observations (like the long-range observations conducted by *New Horizons*; A. J. Verbiscer et al. 2022), until Varda's heliocentric motion brings it to a more favorable viewing geometry. If not tidally relaxed, non-Keplerian shape effects may also provide interesting constraints on Varda's shape, though any constraints will require assumptions about Varda's interior structure (B. C. N. Proudfoot et al. 2024a).

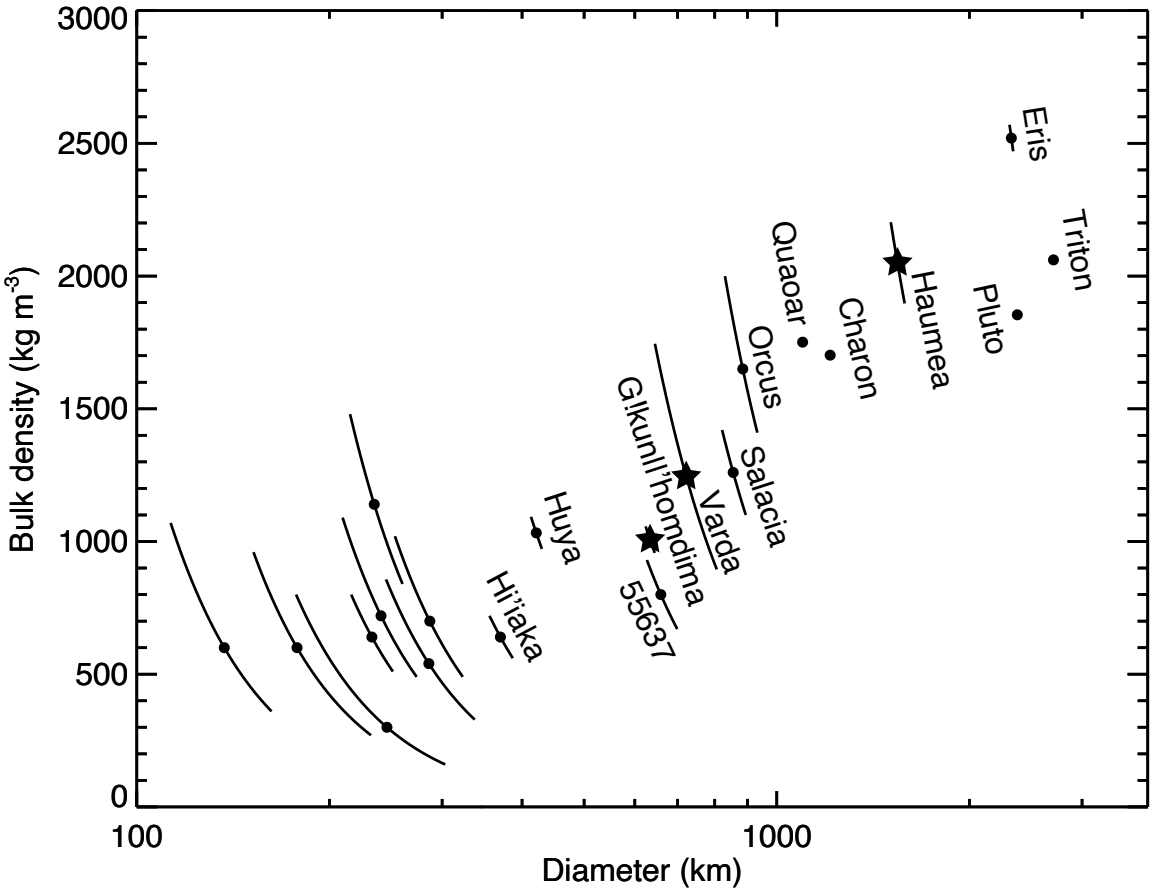

Figure 5. The size–density relationship of TNOs. Sizes/densities updated here are shown by stars. For Varda, we use previous size/density measurements (W. M. Grundy et al. 2015) along with our new system mass. Other densities are from B. Proudfoot et al. (2025), F. L. Rommel et al. (2025), W. M. Grundy et al. (2019), E. Fernández-Valenzuela et al. (2025), and references therein. Unlabeled data points from lower left to upper right are Typhon, Teharonhiawako, Altjira, Ceto, Sila, Lempo, (612239), and (26308).

6. Discussion and Conclusions

The densities of midsized and large TNOs is of utmost importance for understanding the formation, composition, and evolution of TNOs (W. M. Grundy et al. 2019; M. H. Cañas et al. 2024). Indeed, several works have used the distribution of TNO densities to infer the composition and timing of TNO formation (e.g., A. C. Barr & M. E. Schwamb 2016; C. J. Bierson & F. Nimmo 2019). Here, we have shown that by performing a holistic analysis of TNO occultations, light curves, and satellite orbits, we can provide more precise measurements of the density of TNOs. We show these updated densities in Figure 5.

The most obvious interpretation of density variation is distinct compositional differences between objects, where planetary bodies born in certain regions of the protosolar disk may have inherited different initial inventories of ices and refractory materials (M. E. Brown 2013a). One interesting model, which uses both icy and rocky pebbles in a streaming instability and pebble accretion simulation, found that larger planetesimals that undergo pebble accretion will become rockier over time (M. H. Cañas et al. 2024). The model posits that smaller pebbles are more likely to have their ices depleted by UV irradiation, and these pebbles are preferentially incorporated into TNOs via pebble accretion, and provide a good match to the TNO size–density relationship.

In contrast, many evolutionary processes are also likely to shape the densities of TNOs. Collapse of pore space appears to be an important process (W. B. McKinnon et al. 2008; C. J. Bierson & F. Nimmo 2019). Differentiation and internal melting can speed this process, allowing liquid to fill macroscopic porosity (W. B. McKinnon et al. 2008). On the other hand, collisions may also be able to strip outer, less dense layers of a TNO leaving a more dense remnant (e.g., A. C. Barr & M. E. Schwamb 2016).

With a variety of competing models, no agreement has yet been reached on the exact cause of the size–density relation of TNOs. The solution, however, is likely to be multifaceted, with a variety of complex formational and evolutionary processes contributing. Hopefully, more comprehensive models that combine many of these processes can further illuminate the source of the density dichotomy. Likewise, an improvement in the density determinations of TNOs will enable higher confidence in density trends (W. Lyra 2025).

Past a broader look at the ensemble of TNO densities, individual densities are also important for understanding the interiors of TNOs. Densities allow a rough determination of the icy and rocky inventories, and therefore sources of long-term radiogenic heating (A. H. Parker 2021). Larger, denser TNOs have far greater inventories of radionuclides, allowing for more extensive melting and a greater potential for subsurface oceans (S. J. Desch et al. 2009). These bodies have also probably undergone either partial or full differentiation, allowing for formation of a dense rocky core and a water-rich mantle. In these bodies, geochemical processes may be active, producing the methane rich surfaces seen on Pluto, Eris, and Makemake

(C. R. Glein et al. 2024; W. M. Grundy et al. 2024). Smaller, less dense TNOs like G!kún||'hòmdímà likely have never had widespread subsurface melting and remain largely undifferentiated bodies (W. M. Grundy et al. 2019).

Determining shapes is also critical for understanding TNOs. Most clearly, without a precise determination of the shape of a TNO, its density remains poorly constrained, as in the case of Varda (see Section 5). Beyond that, however, shape is an important measurement for a variety of phenomena. Most notably, a secure determination of hydrostatic equilibrium requires precise knowledge of a TNO's shape (G. Tancredi & S. Favre 2008). Shape can also reveal the inner structure of a TNO, as hydrostatic equilibrium shapes are different for nonhomogenous interiors (N. Rambaux et al. 2017; E. T. Dunham et al. 2019). Relatively little is known about the shapes of the largest TNOs, and with increasing numbers of precise stellar occultation observations, we will begin to illuminate the shape distribution of TNOs.

We note that there are significant difficulties in assuming simple hydrostatic equilibrium shapes of TNOs (K. A. Holsapple 2007; E. T. Dunham et al. 2019). Although Jacobi and Maclaurin shapes provide a starting point toward understanding TNO shapes, various complications like viscosity, strength, friction, and nonhomogeneous interiors make them *imperfect* shape models. With the explosion of occultation science, we are quickly approaching a regime where simple models should be abandoned for empirically determined shape models and realistic theoretical models motivated by reasonable geophysical parameters (E. T. Dunham et al. 2019).

To help ascertain both triaxial shapes and densities, we have developed `occult3d`, which is able to flexibly explore shape models of TNOs. The flexibility of a Bayesian parameter inference approach allows `occult3d` to flexibly incorporate a variety of physical constraints, which we have shown can vastly improve triaxial shape models of TNOs. To provide this ability to the community, we have made `occult3d` publicly available, and plan on various upgrades as occultation science progresses. These upgrades will add functionality to fit multiple occultations, focus on hydrostatic equilibrium figures, and add more realistic surface photometric behavior.

We encourage ongoing observations of TNOs, whether long-term photometric monitoring, occultation observations, or continued tracking of TNO satellites. Holistic analyses using all these observations can provide in-depth views into these distant, icy worlds.

Acknowledgments

We thank Bryan Holler for helpful discussions that supported this work. We thank two anonymous reviewers for their feedback that improved the readability of the manuscript. We also thank the BYU Office of Research Computing for their dedication to providing computing resources without which this work would not have been possible. Additionally, we thank the numerous occultation observers involved in originally observing these occultations.

The authors wish to recognize and acknowledge the very significant cultural role and reverence that the summit of Maunakea has always had within the Native Hawaiian community. We are most fortunate to have the opportunity to conduct observations from this mountain.

Some of the data presented herein were obtained at Keck Observatory, which is a private 501(c)3 nonprofit organization operated as a scientific partnership among the California Institute of Technology, the University of California, and the National Aeronautics and Space Administration. The Observatory was made possible by the generous financial support of the W. M. Keck Foundation.

B.P. and F.L.R. acknowledge the generous support of the UCF Preeminent Postdoctoral Program (P^3).

Author Contributions

B.P. was responsible for development, testing, and using `occult3d`, and was primarily responsible for writing the text of the article. W.G. conducted Keck observations of Varda-Ilmarë and conducted preliminary orbit fitting for that system. F.L.R. gave extensive feedback on occultation limb fitting. D.R. provided access to computational resources for the orbit fitting. E.F.-V. supervised B.P. and provided training on understanding occultations. All authors provided editing, commentary, and feedback on the manuscript.

Appendix A
Orbit Fit Diagnostic Plots

In Figures A1 and A2, we show the orbit fit residuals and the orbit fit posterior (as a corner plot).

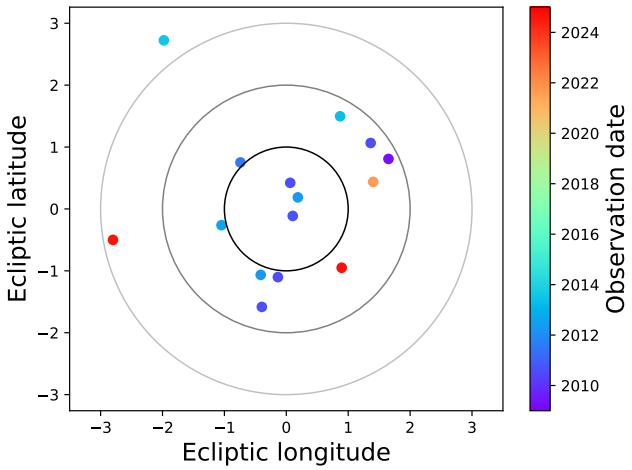

Figure A1. Residuals for the Varda-Ilmarë orbit fit. Circles show the 1σ, 2σ, and 3σ contours. The χ^2 per degree of freedom for this fit is $\sim$1.8.

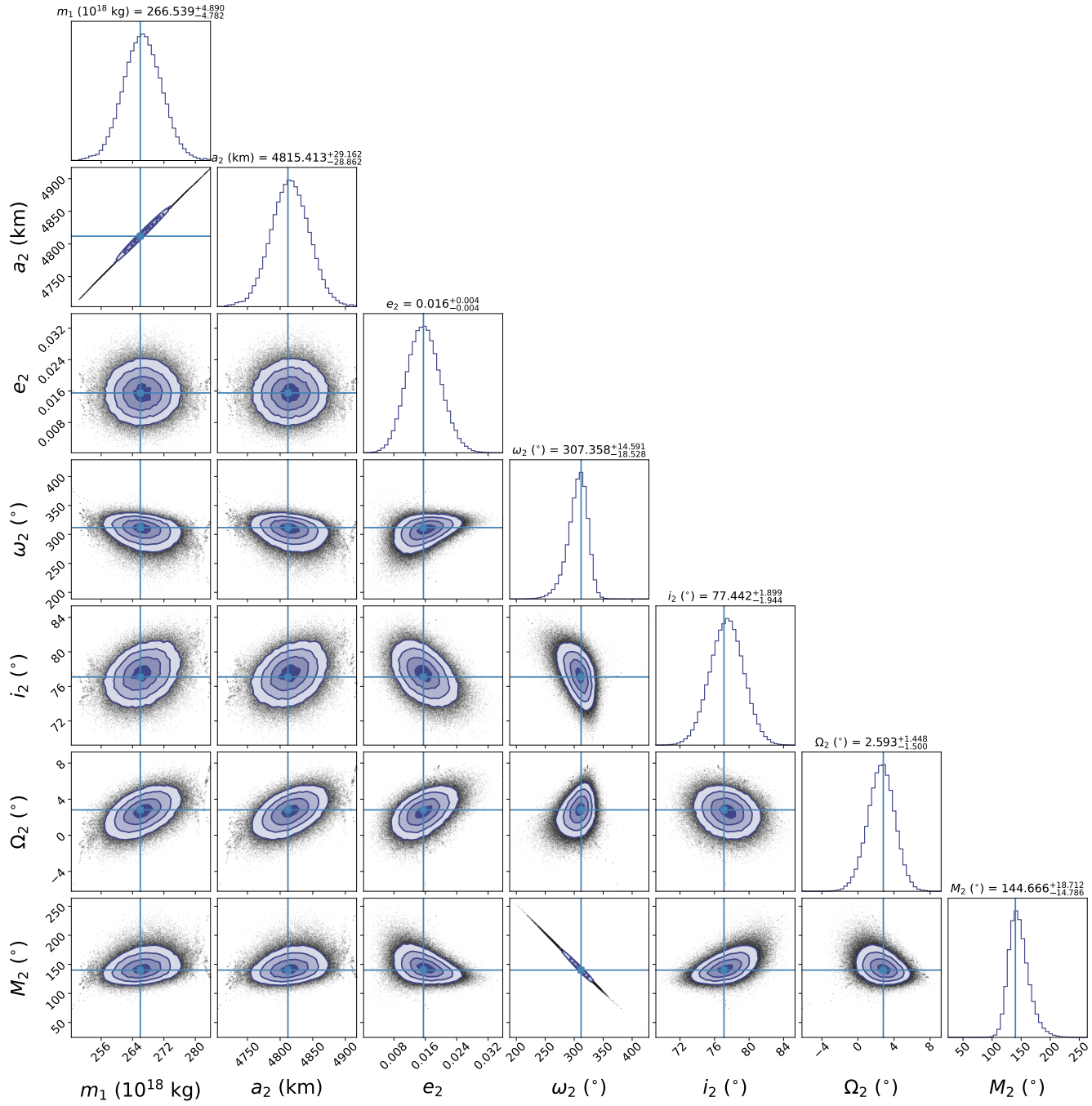

Figure A2. Corner plot for our Keplerian orbit fit of Varda-Ilmarë. Horizontal/vertical lines show the values of the best-fit parameter set. All angles are referenced to the J2000 ecliptic frame.

Appendix B
Occultation Chords

Below, in Table B1, we list all occultation chords used in our shape fitting.

Table B1
Occultation Chords

Site Name	Longitude Latitude Altitude (m)	Immersion Time	Emersion Time	References
G!kún||'hòmdímà, 2014-11-15				
Reno	−119 45 53.0 +39 23 28.5 1470	10:19:34.10 ± 0.70	10:19:46.64 ± 0.65	G. Benedetti-Rossi et al. (2016)
Carson City (B)	−119 47 46.8 +39 11 08.2 1548.1	10:19:32.20 ± 0.50	10:19:47.30 ± 0.41	G. Benedetti-Rossi et al. (2016)
Carson City (S)	−119 33 31.4 +39 16 26.5 1332.6	10:19:30.60 ± 0.60	10:19:46.30 ± 0.42	G. Benedetti-Rossi et al. (2016)
Garderville	−119 40 20.3 +38 53 23.5 1534.9	10:19:29.71 ± 0.46	10:19:48.07 ± 0.30	G. Benedetti-Rossi et al. (2016)
Yerington	−119 09 39.0 +38 59 28.3 1342.7	10:19:29.25 ± 0.41	10:19:46.00 ± 0.35	G. Benedetti-Rossi et al. (2016)
Tonopah	−117 14 06.7 +38 05 22.1 1838.7	10:19:17.6 ± 0.55	10:19:42.45 ± 0.30	G. Benedetti-Rossi et al. (2016)
Urbana	−88 11 46.4 +40 05 12.5 227	10:18:03.61 ± 0.90	10:18:27.60 ± 0.90	G. Benedetti-Rossi et al. (2016)
Adler Springs	−119 24 45.0 +37 04 13.5 1405	10:19:24.356 ± 0.159	10:19:50.249 ± 0.159	K. Schindler et al. (2017)
Varda, 2018-09-10				
MHV	−114 35 48.9 +35 01 54.1 184	03:32:57.10 ± 0.60	03:33:58.83 ± 0.60	D. Souami et al. (2020)
TWF	−114 28 13.1 +42 35 01.9 1133	03:33:56.99 ± 0.76	03:35:05.27 ± 0.30	D. Souami et al. (2020)
YMA	−114 26 10.5 +32 39 34.0 97	03:34:17.10 ± 0.60	03:35:26.39 ± 0.59	D. Souami et al. (2020)
CAR	−111 57 07.9 +33 48 42.9 654	03:34:12.39 ± 0.47	03:35:19.52 ± 0.47	D. Souami et al. (2020)
FLO	−111 21 00.6 +33 00 54.3 484	03:34:23.30 ± 0.13	03:35:26.75 ± 0.15	D. Souami et al. (2020)
Haumea, 2017-01-21				
Skalnate Pleso Observatory	+20 14 02.1 +49 11 21.8 1826	03:08:26.79 ± 0.96	03:10:24.56 ± 0.8	J. L. Ortiz et al. (2017)

Table B1
(Continued)

Site Name	Longitude Latitude Altitude (m)	Immersion Time	Emersion Time	References
Konkoly Observatory (1.0 m)	+19 53 41.5 +47 55 01.6 935	03:08:20.3 ± 0.2	03:10:17.39 ± 0.07	J. L. Ortiz et al. (2017)
Konkoly Observatory (0.6 m)	+19 53 41.5 +47 55 01.6 935	03:08:19.5 ± 0.8	03:10:16.4 ± 1.3	J. L. Ortiz et al. (2017)
Ondrejov Observatory	+14 46 53.3 +49 54 32.6 526	03:08:29.2 ± 0.8	03:10:12.2 ± 0.8	J. L. Ortiz et al. (2017)
Wendelstein Observatory (2.0 m)	+12 00 44.0 +47 42 13.6 1838	03:08:27.9 ± 2.8	03:09:34.1 ± 0.5	J. L. Ortiz et al. (2017)
Wendelstein Observatory (0.4 m)	+12 00 44.0 +47 42 13.6 1838	03:08:18.8 ± 6	03:09:38.6 ± 6	J. L. Ortiz et al. (2017)
Bavarian Public Observatory	+11 36 25.2 +48 07 19.2 538	03:08:30.0 ± 3.3	03:09:30.0 ± 4.9	J. L. Ortiz et al. (2017)
Asiago Observatory	+11 34 08.4 +45 50 54.9 1376	03:08:20.17 ± 0.08	03:09:13.27 ± 1.5	J. L. Ortiz et al. (2017)
San Marcello Pistoiese Observatory	+10 48 14.0 +44 03 51.0 965	03:08:22.9 ± 0.9	03:08:42.8 ± 0.9	J. L. Ortiz et al. (2017)
Lajatico Astronomical Centre	+10 43 01.2 +43 25 44.7 433	03:08:19.9 ± 1.4	03:08:34.3 ± 1.4	J. L. Ortiz et al. (2017)
Mount Agliale Observatory	+10 30 53.8 +43 59 43.1 758	⋯	⋯	J. L. Ortiz et al. (2017)

Note. Longitude is positive to the east and latitude is positive north. Occultation chords with no immersion or emersion times are close negative chords, which are used to filter out two-dimensional ellipses that intersect it.

ORCID iDs

Benjamin Proudfoot https://orcid.org/0000-0002-1788-870X
Will Grundy https://orcid.org/0000-0002-8296-6540
Flavia Luane Rommel https://orcid.org/0000-0002-6085-3182
Estela Fernández-Valenzuela https://orcid.org/0000-0003-2132-7769
Darin Ragozzine https://orcid.org/0000-0003-1080-9770

References

Barr, A. C., & Schwamb, M. E. 2016, Interpreting the Densities of the Kuiper Belt's Dwarf Planets, MNRAS, 460, 1542
Benedetti-Rossi, G., Sicardy, B., Buie, M. W., et al. 2016, Results from the 2014 November 15th Multi-chord Stellar Occultation by the TNO (229762) 2007 UK_{126}, AJ, 152, 156
Bierson, C. J., & Nimmo, F. 2019, Using the Density of Kuiper Belt Objects to Constrain their Composition and Formation History, Icar, 326, 10
Braga-Ribas, F., Vachier, F., Desmars, J., Margoti, G., & Sicardy, B. 2025, Investigating the Formation of Small Solar System Objects Using Stellar Occultations by Satellites: Present, Future and its use to Update Satellite Orbits, RSPTA, 383, 20240200
Brown, M. E. 2013a, The Density of Mid-sized Kuiper Belt Object 2002 UX25 and the Formation of the Dwarf Planets, ApJL, 778, L34
Brown, M. E. 2013b, On the Size, Shape, and Density of Dwarf Planet Makemake, ApJL, 767, L7
Brown, M. E., & Butler, B. J. 2017, The Density of Mid-sized Kuiper Belt Objects from ALMA Thermal Observations, AJ, 154, 19
Brozović, M., Showalter, M. R., Jacobson, R. A., & Buie, M. W. 2015, The Orbits and Masses of Satellites of Pluto, Icar, 246, 317
Buie, M. W., Grundy, W. M., Young, E. F., Young, L. A., & Stern, S. A. 2010, Pluto and Charon with the Hubble Space Telescope. II. Resolving Changes on Pluto's Surface and a Map for Charon, AJ, 139, 1128
Cañas, M. H., Lyra, W., Carrera, D., et al. 2024, A Solution for the Density Dichotomy Problem of Kuiper Belt Objects with Multispecies Streaming Instability and Pebble Accretion, PSJ, 5, 55
Chandrasekhar, S. 1963, The Equilibrium and the Stability of the Roche Ellipsoids, ApJ, 138, 1182
Chandrasekhar, S. 1987, Ellipsoidal Figures of Equilibrium (Dover)
Collyer, C., Fernández-Valenzuela, E., Ortiz, J. L., et al. 2025, Synchronous Rotation in the (120347) Salacia-Actaea System, PSJ, 6, 270
Darwin, G. H. 1886, On Jacobi's Figure of Equilibrium for a Rotating Mass of Fluid, RSPS, 41, 319
Desch, S. J., Cook, J. C., Doggett, T. C., & Porter, S. B. 2009, Thermal Evolution of Kuiper Belt Objects, with Implications for Cryovolcanism, Icar, 202, 694

Desmars, J., Camargo, J. I. B., Braga-Ribas, F., et al. 2015, Orbit Determination of Trans-Neptunian Objects and Centaurs for the Prediction of Stellar Occultations, A&A, 584, A96
Dunham, E. T., Desch, S. J., & Probst, L. 2019, Haumea's Shape, Composition, and Internal Structure, ApJ, 877, 41
Fernández-Valenzuela, E. 2022, Modeling Long-Term Photometric Data of Trans-Neptunian Objects and Centaurs, FrASS, 9, 796004
Fernández-Valenzuela, E., Ortiz, J. L., Duffard, R., Morales, N., & Santos-Sanz, P. 2017, Physical Properties of Centaur (54598) Bienor from Photometry, MNRAS, 466, 4147
Fernández-Valenzuela, E., Ortiz, J. L., Holler, B. J., et al. 2025, Accurate Geometric Albedo, Shape, and Size of Hi'iaka from a Stellar Occultation, NatCo, 16, 10926
Fernández-Valenzuela, E., Ortiz, J. L., Morales, N., et al. 2019, The Changing Rotational Light-curve Amplitude of Varuna and Evidence for a Close-in Satellite, ApJL, 883, L21
Foreman-Mackey, D., Conley, A., Meierjurgen Farr, W., et al. 2013, emcee: The MCMC Hammer, Astrophysics Source Code Library, ascl:1303.002
Fuentes-Muñoz, O., Farnocchia, D., Giorgini, J. D., & Park, R. S. 2025, Asteroid Mass Estimation by Mutual Perturbations During Close Encounters After Gaia Focused Product Release, AJ, 170, 353
Gaia Collaboration, Vallenari, A., Brown, A. G. A., et al. 2023, Gaia Data Release 3. Summary of the Content and Survey Properties, A&A, 674, A1
Glein, C. R., Grundy, W. M., Lunine, J. I., et al. 2024, Moderate D/H Ratios in Methane Ice on Eris and Makemake as Evidence of Hydrothermal or Metamorphic Processes in their Interiors: Geochemical Analysis, Icar, 412, 115999
Gomes-Júnior, A. R., Morgado, B. E., Benedetti-Rossi, G., et al. 2022, SORA: Stellar Occultation Reduction and Analysis, MNRAS, 511, 1167
Grundy, W. M., Noll, K. S., Buie, M. W., et al. 2019, The Mutual Orbit, Mass, and Density of Transneptunian Binary G!kún||'hòmdímà(229762 2007 UK_{126}), Icar, 334, 30
Grundy, W. M., Porter, S. B., Benecchi, S. D., et al. 2015, The Mutual Orbit, Mass, and Density of the lArge Transneptunian Binary System Varda and Ilmarë, Icar, 257, 130
Grundy, W. M., Wong, I., Glein, C. R., et al. 2024, Measurement of D/H and $^{13}C/^{12}C$ Ratios in Methane Ice on Eris and Makemake: Evidence for Internal Activity, Icar, 411, 115923
Guilbert-Lepoutre, A., Prialnik, D., & Métayer, R. 2020, in The Trans-Neptunian Solar System, ed. D. Prialnik, M. A. Barucci, & L. Young (Elsevier), 183
Holsapple, K. A. 2007, Spin Limits of Solar System Bodies: From the Small Fast-rotators to 2003 EL61, Icar, 187, 500
Hussmann, H., Sohl, F., & Spohn, T. 2006, Subsurface Oceans and Deep Interiors of Medium-sized Outer Planet Satellites and Large Trans-neptunian Objects, Icar, 185, 258
Hut, P. 1980, Stability of Tidal Equilibrium, A&A, 92, 167
Johnson, T. V., & McGetchin, T. R. 1973, Topography on Satellite Surfaces and the Shape of Asteroids, Icar, 18, 612
Kiss, C., Marton, G., Parker, A. H., et al. 2019, The Mass and Density of the Dwarf Planet (225088) 2007 OR_{10}, Icar, 334, 3
Kretlow, M., Ortiz, J. L., Desmars, J., et al. 2024, Physical Properties of Trans-Neptunian object (143707) 2003 UY_{117} Derived from Stellar Occultation and Photometric Observations, A&A, 691, A31
Lacerda, P., Jewitt, D., & Peixinho, N. 2008, High-Precision Photometry of Extreme KBO 2003 EL_{61}, AJ, 135, 1749
Leinhardt, Z. M., Marcus, R. A., & Stewart, S. T. 2010, The Formation of the Collisional Family Around the Dwarf Planet Haumea, ApJ, 714, 1789
Lellouch, E., Santos-Sanz, P., Lacerda, P., et al. 2013, "TNOs are Cool": A Survey of the Trans-Neptunian Region. IX. Thermal Properties of Kuiper Belt Objects and Centaurs from Combined Herschel and Spitzer Observations, A&A, 557, A60
Leone, G., Paolicchi, P., Farinella, P., & Zappala, V. 1984, Equilibrium Models of Binary Asteroids, A&A, 140, 265
Lockwood, A. C., Brown, M. E., & Stansberry, J. 2014, The Size and Shape of the Oblong Dwarf Planet Haumea, EM&P, 111, 127
Loveless, S., Prialnik, D., & Podolak, M. 2022, On the Structure and Long-term Evolution of Ice-rich Bodies, ApJ, 927, 178
Lyra, W. 2025, Where are the Missing Kuiper Belt Binaries?, Icar, 442, 116737
Magnusson, P. 1986, Distribution of Spin Axes and Senses of Rotation for 20 Large Asteroids, Icar, 68, 1
Margoti, G., et al. 2024, Master's thesis, Universidade Tecnológica Federal do Paraná
Marzari, F. 2020, Ring Dynamics Around an Oblate Body with an Inclined Satellite: The Case of Haumea, A&A, 643, A67
McKinnon, W. B., Prialnik, D., Stern, S. A., & Coradini, A. 2008, Structure and Evolution of Kuiper Belt Objects and Dwarf Planets (Univ. Arizona Press), 213
Milbury, C., Johnson, B. C., Melosh, H. J., et al. 2015, Preimpact Porosity Controls the Gravity Signature of Lunar Craters, GeoRL, 42, 9711
Morbidelli, A., & Nesvorný, D. 2020, in The Trans-Neptunian Solar System, ed. D. Prialnik, M. A. Barucci, & L. Young (Elsevier), 25
Morgado, B. E., Sicardy, B., Braga-Ribas, F., et al. 2021, Refined Physical Parameters for Chariklo's Body and Rings from Stellar Occultations Observed between 2013 and 2020, A&A, 652, A141
Müller, T., Lellouch, E., & Fornasier, S. 2020, in The Trans-Neptunian Solar System, ed. D. Prialnik, M. A. Barucci, & L. Young (Elsevier), 153
Nelsen, M. A., Ragozzine, D., Proudfoot, B. C. N., Giforos, W. G., & Grundy, W. 2025, Beyond Point Masses. IV. Trans-Neptunian Object Altjira Is Likely a Hierarchical Triple Discovered through Non-Keplerian Motion, PSJ, 6, 53
Ortiz, J. L., Santos-Sanz, P., Sicardy, B., et al. 2017, The Size, Shape, Density and Ring of the Dwarf Planet Haumea from a Stellar Occultation, Natur, 550, 219
Ortiz, J. L., Sicardy, B., Braga-Ribas, F., et al. 2012, Albedo and Atmospheric Constraints of Dwarf Planet Makemake from a Stellar Occultation, Natur, 491, 566
Ortiz, J. L., Sicardy, B., Camargo, J. I. B., Santos-Sanz, P., & Braga-Ribas, F. 2020, in The Trans-Neptunian Solar System, ed. D. Prialnik, M. A. Barucci, & L. Young (Elsevier), 413
Parker, A. H. 2021, in The Pluto System After New Horizons, ed. S. A. Stern et al. (Univ. Arizona Press), 545
Proudfoot, B., Grundy, W., Ragozzine, D., & Fernández-Valenzuela, E. 2025, Beyond Point Masses. V. Weywot's Non-Keplerian Orbit, PSJ, 6, 285
Proudfoot, B. C. N., Ragozzine, D. A., Giforos, W., et al. 2024a, Beyond Point Masses. III. Detecting Haumea's Nonspherical Gravitational Field, PSJ, 5, 69
Proudfoot, B. C. N., Ragozzine, D. A., Thatcher, M. L., et al. 2024b, Beyond Point Masses. II. Non-Keplerian Shape Effects Are Detectable in Several TNO Binaries, AJ, 167, 144
Ragozzine, D., Pincock, S., Proudfoot, B. C. N., et al. 2024, arXiv:2403.12785
Rambaux, N., Baguet, D., Chambat, F., & Castillo-Rogez, J. C. 2017, Equilibrium Shapes of Large Trans-Neptunian Objects, ApJL, 850, L9
Rizos, J. L., Ortiz, J. L., Rommel, F. L., et al. 2025, The Trans-Neptunian Object (119951) 2002 KX14 Revealed via Multiple Stellar Occultations, A&A, 697, A62
Roche, É. 1850, La Figure d'une Masse Fluide, Vol. 1 (Memoires de l'Acad), 333, émie de Montpellier
Rommel, F. L., Braga-Ribas, F., Ortiz, J., et al. 2023, A Large Topographic Feature on the Surface of the Trans-Neptunian Object (307261) 2002 MS4 Measured from Stellar Occultations, A&A, 678, A167
Rommel, F. L., Fernández-Valenzuela, E., Proudfoot, B. C. N., et al. 2025, Stellar Occultation Observations of (38628) Huya and Its Satellite: A Detailed Look into the System, PSJ, 6, 48
Schaller, E. L., & Brown, M. E. 2007, Volatile Loss and Retention on Kuiper Belt Objects, ApJL, 659, L61
Schindler, K., Bosh, A. S., Levine, S. E., et al. 2019, Results from a stellar occultation by KBO Varda, AGUFM, 2019, P42C–08
Schindler, K., Wolf, J., Bardecker, J., et al. 2017, Results from a Triple Chord Stellar Occultation and Far-infrared Photometry of the Trans-Neptunian Object (229762) 2007 UK_{126}, A&A, 600, A12
Sheppard, S. S., Lacerda, P., & Ortiz, J. L. 2008, in The Solar System Beyond Neptune, ed. M. A. Barucci et al. (Univ. Arizona Press), 129
Sicardy, B., Braga-Ribas, F., Buie, M. W., Ortiz, J. L., & Roques, F. 2024, Stellar Occultations by Trans-Neptunian Objects, A&ARv, 32, 6
Sicardy, B., Ortiz, J. L., Assafin, M., et al. 2011, A Pluto-like Radius and a High Albedo for the Dwarf Planet Eris from an Occultation, Natur, 478, 493
Souami, D., Braga-Ribas, F., Sicardy, B., et al. 2020, A multi-chord Stellar Occultation by the Large Trans-Neptunian Object (174567) Varda, A&A, 643, A125
Stern, S. A., Buie, M. W., & Trafton, L. M. 1997, HST High-Resolution Images and Maps of Pluto, AJ, 113, 827

Tancredi, G., & Favre, S. 2008, Which are the Dwarfs in the Solar System?, Icar, 195, 851
Tegler, S. C., Romanishin, W., Consolmagno, G. J., et al. 2005, The Period of Rotation, Shape, Density, and Homogeneous Surface Color of the Centaur 5145 Pholus, Icar, 175, 390
Thirouin, A., Noll, K. S., Ortiz, J. L., & Morales, N. 2014, Rotational Properties of the Binary and Non-binary Populations in the Trans-Neptunian Belt, A&A, 569, A3
Thirouin, A., Ortiz, J. L., Duffard, R., et al. 2010, Short-term Variability of a Sample of 29 Trans-Neptunian Objects and Centaurs, A&A, 522, A93
Tholen, D. J., & Tedesco, E. F. 1994, Pluto's Lightcurve: Results from Four Oppositions, Icar, 108, 200
Thompson, I. 2011, NIST Handbook of Mathematical Functions, Edited by Frank W.J. Olver, Daniel W. Lozier, Ronald F. Boisvert, Charles W. Clark, ConPh, 52, 497
Tiscareno, M. S. 2013, in Planets, Stars and Stellar Systems. Volume 3: Solar and Stellar Planetary Systems, ed. T. D. Oswalt, L. M. French, & P. Kalas (Springer), 309
Verbiscer, A. J., Helfenstein, P., Porter, S. B., et al. 2022, The Diverse Shapes of Dwarf Planet and Large KBO Phase Curves Observed from New Horizons, PSJ, 3, 95
Wizinowich, P. L., Le Mignant, D., Bouchez, A. H., et al. 2006, The W. M. Keck Observatory Laser Guide Star Adaptive Optics System: Overview, PASP, 118, 297